Solar Energy Materials & Solar Cells 95 (2011) 921–926

Contents lists available at ScienceDirect

Solar Energy Materials & Solar Cells

journal homepage: www.elsevier.com/locate/solmat

Optimization of inverted tandem organic solar cells

D.W. Zhao [a,b], L. Ke [c], Y. Li [d], S.T. Tan [a], A.K.K. Kyaw [a], H.V. Demir [a], X.W. Sun [a,e,*], D.L. Carroll [d,**], G.Q. Lo [b], D.L. Kwong [b]

[a] School of Electrical and Electronic Engineering, Nanyang Technological University, Nanyang Avenue, Singapore 639798, Singapore
[b] Institute of Microelectronics, A*STAR (Agency for Science, Technology and Research), 11 Science Park Road, Science Park II, Singapore 117685, Singapore
[c] Institute of Materials Research and Engineering, A*STAR (Agency for Science, Technology and Research), 3 Research Link, Singapore 117602, Singapore
[d] Center for Nanotechnology and Molecular Materials, Department of Physics, Wake Forest University, Winston-Salem, NC 27109, USA
[e] Department of Applied Physics, College of Science, Tianjin University, Tianjin 300072, China

ARTICLE INFO

Article history:
Received 8 October 2010
Received in revised form
22 November 2010
Accepted 24 November 2010
Available online 18 December 2010

Keywords:
Tandem organic solar cells
Inverted structure
Intermediate layer
Buffer layer

ABSTRACT

Inverted tandem organic solar cells, consisting of two bulk heterojunction sub-cells with identical poly(3-hexylthiophene) (P3HT) and 1-(3-methoxycarbonyl)-propyl-1-phenyl-(6,6)C_{61} (PCBM) active layer and a MoO_3/Ag/Al/Ca intermediate layer, have been presented and optimized. Indium tin oxide (ITO) modified by Ca acts as a cathode for electron collection and Ag is used as the anode for hole collection for the tandem device. A proper thickness of Ca (3 nm) forms a continuous layer, working as a cathode for the top sub-cell. MoO_3 as the anode buffer layer prevents exciton quenching and charge loss at the anode side, which could result in increase in interfacial resistance. The variance of sub-cell thickness adjusts the optical field distribution in the entire device, facilitating light absorption and good current matching in both sub-cells. The optimal inverted tandem device achieves a maximum power conversion efficiency of 2.89% with a short-circuit current density of 4.19 mA/cm^2, an open-circuit voltage of 1.17 V, and a fill factor of 59.0% under simulated 100 mW/cm^2 (AM 1.5G) solar irradiation.

1. Introduction

Investigation on organic solar cells (OSCs) has intensified in the past few years due to greatly increased demands for green energy and their unique properties compared to inorganic solar cells [1–7]. A few intrinsic properties of organic semiconductors, such as their narrow absorption range, short exciton diffusion length, and low charge carrier mobility, limit the device efficiency [8,9]. The bulk heterojunction (BHJ) structure employed in OSCs exhibits remarkable superiority over single layer or bilayer structures [10–12], primarily due to the decreased exciton diffusion distance to donor/acceptor interfaces and increased interfacial areas, facilitating exciton dissociation and yielding photocurrent enhancement. The charge transport in such a structure depends on the nanoscale bi-continuous percolated pathways, and subsequently the charge carriers can be extracted by their corresponding electrodes [3,13,14]. It has been found that the poly(3-hexylthiophene) (P3HT):1-(3-methoxycarbonyl)-propyl-1-phenyl-(6,6)C_{61} (PCBM) based BHJ exhibits vertical phase separation [12,15], i.e. PCBM-rich at the bottom (ITO anode side) and P3HT-rich atop (cathode side), which obstructs efficient charge transport in conventional devices. The inverted structure with the direction of charge transport/collection reversed (ITO is modified as cathode and a high work function metal is used as anode) is beneficial for charge transport and collection in these circumstances. Moreover, this inverted structure can also overcome the interface instability between poly(3,4-ethylenedioxythiophene):poly(styrenesulfonate) (PEDOT:PSS) and low work function metals in conventional devices [16–22].

On the other hand, in order to improve absorption efficiency, organic materials with lower band gap and broad absorption range have been synthesized [9–11]. In addition, increasing active layer thickness can lead to more solar light absorption. However, the thickness has to be limited to within ~100 nm due to the relatively small charge carrier mobility, which leads to a high recombination rate [23–25]. Therefore, a tandem structure consisting of two or more cells with complementary absorption spectra is believed to have the potential to further boost the efficiency by means of maximization of light absorption [3,26–33]. In conventional tandem devices, intermediate layers are of great significance to effectively connect the sub-cells [30,34], which are usually comprised of metal nanoclusters [29,35], metal/PEDOT:PSS combination [26,36], metal oxides/PEDOT:PSS combination [28,37,38], and metal/metal oxide combination [27,30,31]. However, these

* Corresponding author at: School of Electrical and Electronic Engineering, Nanyang Technological University, Nanyang Avenue, Singapore 639798, Singapore.
** Corresponding author.
E-mail addresses: exwsun@ntu.edu.sg (X.W. Sun), carroldl@wfu.edu (D.L. Carroll).

0927-0248/$ - see front matter © 2010 Elsevier B.V. All rights reserved.
doi:10.1016/j.solmat.2010.11.023

intermediate layers cannot be applied in inverted tandem OSCs, where ITO acts as the cathode at the bottom and the high work function metal atop as the anode.

Recently, we compared the intermediate layers with various combinations of metals and metal oxides used in inverted tandem OSCs [39]. As a result, the combination of a MoO_3 layer and Ag/Al/Ca metal layers has been found to function well as an intermediate layer to efficiently connect two BHJ polymer sub-cells. In this work, we present a detailed study on optimizing the intermediate layer and the two BHJ sub-cell thicknesses through experiments and simulations.

2. Experiment

All cells in this study were fabricated on indium tin oxide (ITO) coated glass substrates with a sheet resistance of 20 Ω/sq. A Ca layer was first thermally evaporated in a base vacuum of 9.0×10^{-5} Pa.

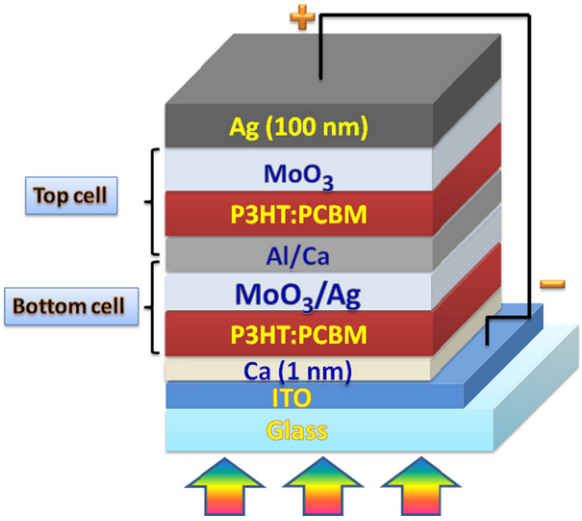

Fig. 1. Device structure of inverted tandem OSCs.

Then, a blend solution made of P3HT (Rieke Metals, Inc.) and PCBM (American Dye Sources Inc.) with a weight ratio of 1:0.8 in chlorobenzene (30 mg/ml) was spin-coated to form the active layers for both bottom and top sub-cells in a glove box filled with N_2. MoO_3, Ag, Al, and Ca were evaporated in sequence to assigned thicknesses to form the intermediate layer (9.0×10^{-5} Pa). Evaporated MoO_3/Ag with a variable thickness of MoO_3 was used as the anode for all tandem cells in this paper. Post-annealing at 160 °C for 10 min was performed on all devices after the final MoO_3/Ag anode fabrication. All devices had an active area of 0.1 cm^2 and were encapsulated before being taken out from the glove box.

The current–voltage (I–V) characteristics were measured with a Keithley 2400 sourcemeter under simulated 100 mW/cm^2 (AM 1.5G) irradiation from a solar simulator (Solar Light Company Inc.). The film thickness was measured with a surface profiler (Tencor P15). A tapping mode atomic force microscope (tapping mode AFM) (D5000, Veeco) was used to characterize the surface roughness of metal oxide layer, metal layers, and spin-coated polymer on Ca coated ITO glass. Fig. 1 shows the structure of the inverted tandem device in this study, consisting of ITO/Ca/P3HT:PCBM/MoO_3/Ag/Al/Ca/P3HT:PCBM/MoO_3/Ag. Devices with variable thicknesses of Ca in the intermediate layer, MoO_3 buffer layer, and P3HT:PCBM active layers in sub-cells were fabricated for comparison.

3. Results and discussion

3.1. Morphology of intermediate layer

Fig. 2 shows the surface morphology (tapping mode AFM images) of P3HT:PCBM (80 nm), P3HT:PCBM (80 nm)/MoO_3 (7.5 nm), P3HT:PCBM (80 nm)/MoO_3 (7.5 nm)/Ag(1 nm), P3HT:PCBM (80 nm)/MoO_3 (7.5 nm)/Ag (1 nm)/Al (1 nm), and P3HT:PCBM (80 nm)/MoO_3 (7.5 nm)/Ag (1 nm)/Al (1 nm)/Ca (3 nm) films used in the inverted tandem cells. The P3HT:PCBM (80 nm) film displays a rather smooth surface with a root-mean-square (RMS) surface roughness of 0.703 nm. Obviously, the deposited MoO_3 layer (7.5 nm) does not cause an increase in surface roughness (0.740 nm). With the deposition of metal layers (Ag, Al, and Ca) used for the intermediate layer, the RMS surface

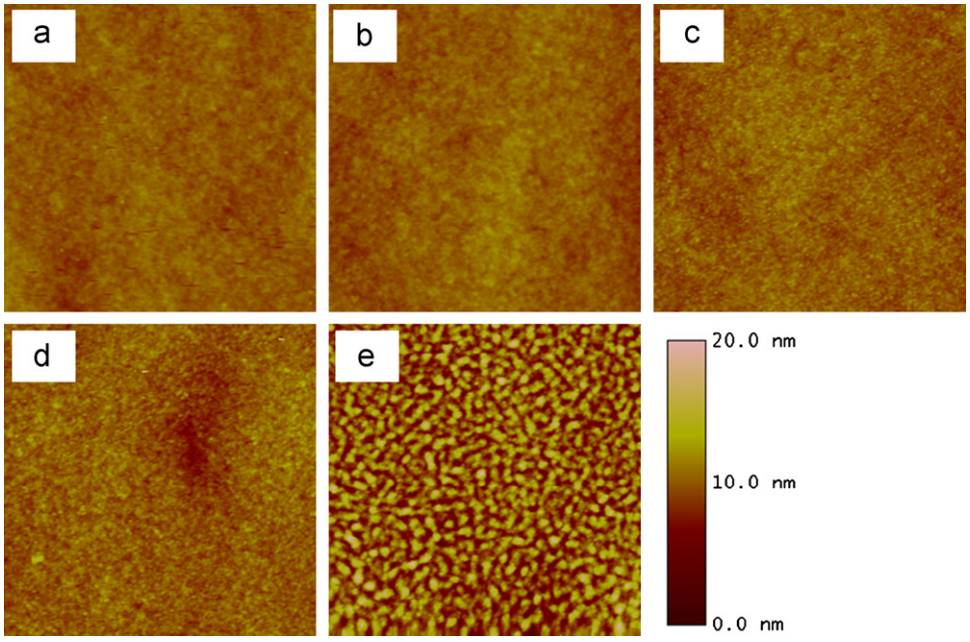

Fig. 2. Surface morphology (AFM images) of different films used for the intermediate layer: (a) P3HT:PCBM, (b) P3HT:PCBM/MoO_3, (c) P3HT:PCBM/MoO_3/Ag, (d) P3HT:PCBM/MoO_3/Ag/Al, and (e) P3HT:PCBM/MoO_3/Ag/Al/Ca.

roughness increases to 0.829, 1.048, and 2.712 nm for P3HT:PCBM/MoO_3/Ag, P3HT:PCBM/MoO_3/Ag/Al, and P3HT:PCBM/MoO_3/Ag/Al/Ca films, respectively. This indicates that ultrathin Ag and Al make the films slightly rougher due to aggregation of metal nanoclusters during their depositions. It has to be pointed out that the AFM measurement was performed in air, leading to oxidization of Ca layer, therefore, the surface roughness of the P3HT:PCBM/MoO_3/Ag/Al/Ca film (2.712 nm) is remarkably higher than those of other films.

3.2. Contributions of components in the intermediate layer

A careful combination of multiple ultrathin metals and metal oxide is essential to realize effective connection of the sub-cells. The MoO_3 layer plays multiple roles in inverted single devices [19,22], including transporting and extracting holes, preventing exciton quenching at the Ag electrode, protecting the active layer from damage caused by Ag deposition, and adjusting the optical field distribution as an optical spacer in the entire device. Hence, the MoO_3 layer thickness significantly influences the device performance. For the intermediate layer in inverted tandem devices, if the MoO_3 layer is too thick, it will cause a high series resistance and a large voltage drop across this layer, leading to reduction in FF and V_{oc} [19,22]. Meanwhile, if the MoO_3 layer is too thin, it cannot completely protect the prior-deposited polymer from being dissolved [30]. Therefore, the optimal thickness of the MoO_3 layer was found to be 7.5 nm, which functions well as both a connecting unit layer working as anode of the bottom sub-cell and a protection layer.

It has been found that the metal layers are also crucial to implement efficient sub-cell connection for good device performance [39]. Table 1 compares the performance of inverted tandem devices with and without Ag or Al layers as part of the intermediate layer [39]. It is obvious that insertion of Ag or Al significantly influences the final FF and V_{oc} of tandem devices, respectively. Without Ag, FF is much lower, indicating larger internal resistance and less efficient charge extraction and recombination at the intermediate layer [39]. On the other hand, the absence of Al results in reduction of V_{oc} to 0.99 V for the tandem cell, smaller than the summation of V_{oc} of the sub-cells. This low V_{oc} is primarily attributed to the energy barrier, causing a large voltage drop across this intermediate layer [39].

Finally, the thickness of Ca, as a part of the intermediate layer for inverted tandem devices, also has great impact on single inverted device performance. For our inverted single devices, the optimal thickness of Ca was found to be between 0.5 and 1 nm [19,22].

Fig. 3 shows the *I–V* characteristics of the inverted tandem cells (80 nm bottom sub-cell and 70 nm top sub-cell) with different thicknesses of Ca in the intermediate layer and 5 nm MoO_3 as a anode buffer layer. Obviously, the V_{ocs} for all devices are similar, indicating that Ca acts effectively as a cathode for the top sub-cell. When the Ca layer is 1.5 and 3 nm, the device has J_{sc} of 3.77 and 4.19 mA/cm^2, respectively. However, the device with 1.5 nm Ca exhibits higher photocurrent variation in the reverse bias region than that with 3 nm Ca, implying the existence of a slightly larger leakage current in the device with 1.5 nm Ca. This might be caused by the relatively thin Ca layer (1.5 nm), which cannot form a continuous film on the prior-deposited multiple layers. However, it can be observed that this 3 nm-thick Ca layer performs well. With further increase in Ca thickness to 4.5 nm, the performance drops dramatically; in particular, we observe a striking drop in FF, implying a large series resistance and bad current matching. As a consequence, the optimal device has a 3 nm Ca layer, exhibiting a PCE of 2.89% with J_{sc}=4.19 mA/cm^2, V_{oc}=1.17 V, and FF=59.0%.

3.3. MoO_3 optimization as anode buffer layer

It is worth mentioning that MoO_3 as an anode buffer layer has a significant influence on inverted single devices with Ca as the electron-transporting layer [19,22]. Hence, it is still necessary to optimize the thickness of MoO_3 as an anode buffer layer in the inverted tandem devices to prevent exciton quenching and charge loss at the anode side. Fig. 4 shows the *I–V* characteristics of the inverted tandem cells under 100 mW/cm^2 with MoO_3/Ag/Al/Ca as the (Ca=3 nm) intermediate layer and variable MoO_3 as the anode buffer layer. When MoO_3 is 3 or 5 nm, the devices have identical V_{oc} of 1.17 V. However, a 7 nm MoO_3 thickness makes the V_{oc} drop to 1.13 V, primarily originating from the slightly reduced V_{oc} in single top cell caused by a relatively thick MoO_3 layer [19,22]. Moreover, the devices with all three thicknesses of MoO_3 exhibit similar FFs of around 59.0%. Since the current matching is obtained in stacked sub-cells for the device with 5 nm MoO_3 [22], the device achieves the best J_{sc} of 4.19 mA/cm^2. Overall, the MoO_3 layer as an anode buffer layer is optimized to be 5 nm, demonstrating that the thickness of MoO_3 layer has a slight effect on inverted tandem device performance.

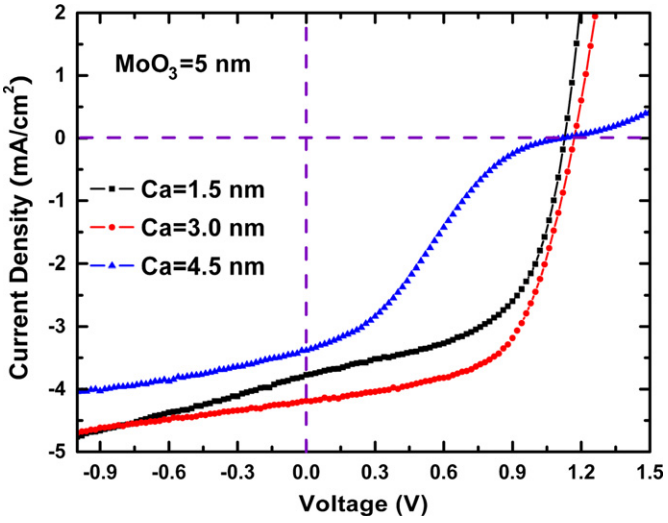

Fig. 3. *I–V* characteristics of the inverted tandem cells with MoO_3/Ag/Al/Ca intermediate layer for varying thickness of Ca and 5 nm MoO_3 as the anode buffer layer under 100 mW/cm^2.

Table 1
Performance comparison of inverted tandem devices with Ag and Al, and with Ag or Al layers in the intermediate layer (MoO_3/Ag (1 nm)/Al (1 nm)/Ca (3 nm), MoO_3/Al (1 nm)/Ca (3 nm) and MoO_3/Ag (1 nm)/Ca (3 nm)).

Intermediate layer combination	J_{sc} (mA/cm^2)	V_{oc} (V)	FF (%)	PCE (%)	Reference
MoO_3/Ag (1 nm)/Al (1 nm)/Ca (3 nm)	4.19	1.17	59.0	2.89	This work
MoO_3/Al (1 nm)/Ca (3 nm)	3.85	1.19	31.2	1.43	[39]
MoO_3/Ag (1 nm)/Ca (3 nm)	3.93	0.99	59.1	2.30	[39]

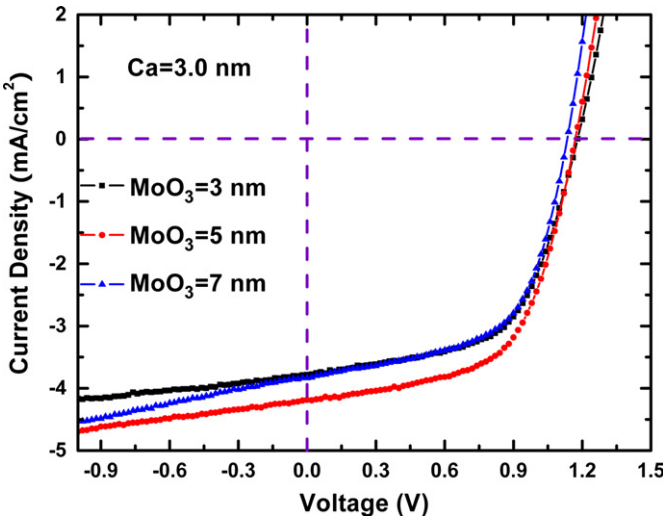

Fig. 4. *I–V* characteristics of the inverted tandem cells under 100 mW/cm^2 with MoO_3/Ag/Al/Ca(5 nm) intermediate layer and variable thickness of MoO_3 anode buffer layer.

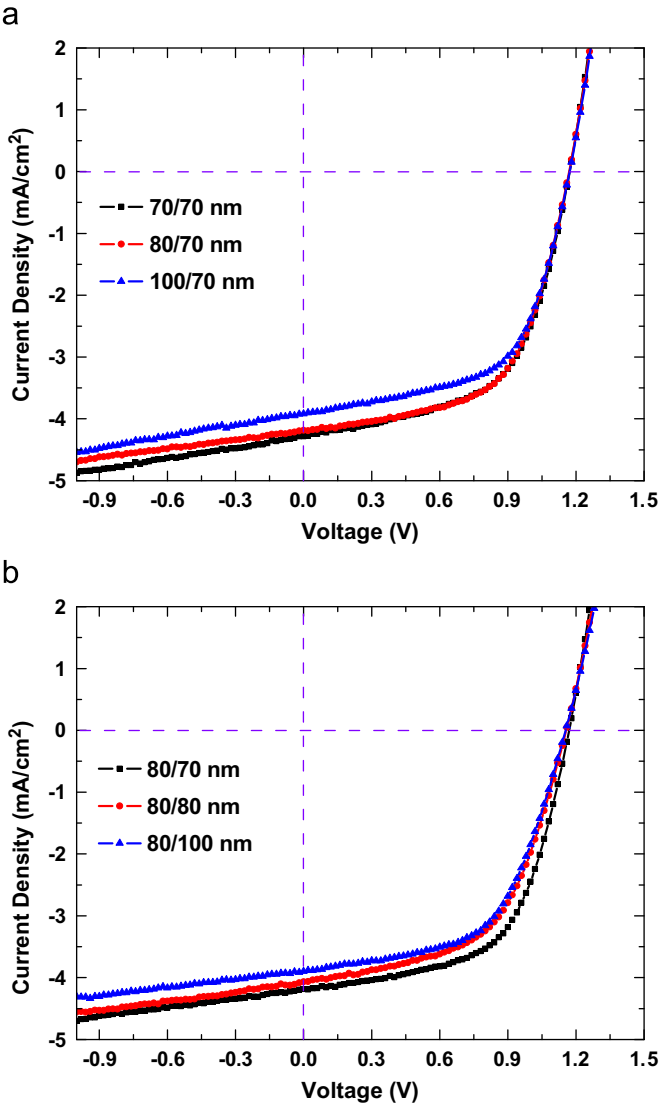

Fig. 5. *I–V* characteristics of the inverted tandem cells under 100 mW/cm^2 with MoO_3/Ag/Al/Ca intermediate layer and different thicknesses of active layers in sub-cells: (a) bottom cell=70, 80, and 100 nm, top cell=70 nm and (b) bottom cell=80 nm, top cell=70, 80, and 100 nm.

3.4. Optimization of sub-cell thickness

For multiple layer based solar cells, the layer thickness determines the light absorption via a change in optical field distribution within the device. Correspondingly, some approaches have been employed to effectively adjust the optical field distribution inside these devices, such as varying layer thickness [22,40–42], introducing an optical spacer that will not affect the initial electrical properties [43–47], and using a highly reflective electrode to enhance the fraction of reflected light [48,49].

The tandem OSC is a typical multiple layer based solar cell, where an optimal PCE can be obtained by changing the thickness of each sub-cell so as to attain good current matching. In order to understand the effect of sub-cell thickness on the final photocurrent, we simulated the optical field distribution in the entire device and calculated the current density contributed by bottom and top sub-cells with different thicknesses using a transfer matrix method [40,50,51]. The overall J_{sc} was set to be the smaller one of the top and bottom sub-cells. For this simulation, complex refractive indexes of various layers were obtained from several sources [50,52–55]. Fig. 6 shows the 3D plot of the overall J_{sc} of inverted tandem cells as functions of bottom and top sub-cell layer thickness [56].

Fig. 5(a) shows the *I–V* characteristics of the inverted tandem cells with a fixed top sub-cell (70 nm) and a variable thickness of bottom sub-cell (70, 80, and 100 nm) under 100 mW/cm^2. With the top sub-cell thickness of 70 nm, J_{sc} of inverted tandem device slightly decreases from 4.28 to 3.92 mA/cm^2 when the bottom sub-cell thickness increases from 70 to 100 nm. This is primarily attributed to the slight variation of optical field distribution, leading to the shift of current matching. This change is consistent with the trend shown in Fig. 6. However, the 70 nm bottom sub-cell has to suffer a relatively high resistance caused by 7.5 nm MoO_3 as an anode buffer layer compared to the 80 and 100 nm bottom sub-cells [22]. Therefore, the inverted tandem device with 70 nm bottom and top sub-cells has a lower FF (57.6%) than those with 80 or 100 nm bottom sub-cell and 70 nm top sub-cell (59.0% and 59.0%, respectively). This is the main reason why the optimal inverted device is obtained by stacking 80 nm bottom and 70 nm top sub-cells. On the other hand, Fig. 5(b) shows the *I–V* characteristics of the inverted tandem cells with a fixed bottom sub-cell

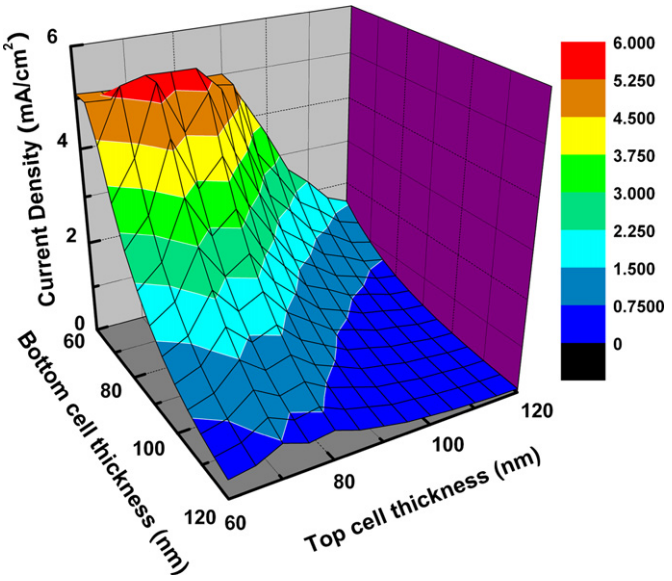

Fig. 6. 3D plot of the overall J_{sc} of the inverted tandem cells versus bottom and top sub-cell layer thicknesses.

(80 nm) and variable thickness of top sub-cell (70, 80, and 100 nm) under 100 mW/cm^2. Similarly, the final photocurrent drops with increase in top sub-cell thickness, exhibiting J_{sc} of 4.19, 4.07, and 3.90 mA/cm^2 for the devices with top sub-cell thickness of 70, 80, and 100 nm, respectively. Fig. 6 shows a similar trend in photocurrent (the trend for 70 and 80 nm sub-cells). These results indicate that the interference effect between the incident light and the reflected light from the metal electrode reduces due to the use of identical active materials in both sub-cells and increase in active layer thickness. As a consequence, the optimized combination for inverted tandem devices is 80 and 70 nm for bottom and top sub-cells, respectively.

4. Conclusion

In conclusion, we have optimized the inverted tandem organic solar cells with a MoO_3/Ag/Al/Ca intermediate layer by tuning the thickness of Ca as part of an intermediate layer, MoO_3 as a buffer layer, and P3HT:PCBM as an active layer. This intermediate layer exhibits slight a change in surface roughness with the deposition of each layer. 3 nm-thick Ca acts well as the cathode for top sub-cell, benefiting to the protection of the prior-deposited active layer. The optimal thickness of MoO_3 anode buffer layer is 5 nm for effectively preventing exciton quenching and damage from Ag deposition. The optical field distribution in the device is tuned by the change in sub-cell thickness for matching photocurrent. Finally, the best device performance is obtained with the 80 nm bottom sub-cell, 70 nm top sub-cell, 3 nm Ca as part of the intermediate layer, and 5 nm MoO_3 anode buffer layer. We anticipate that the proposed intermediate layer could provide an efficient approach to achieve performance improvements in inverted tandem devices with complementary absorbing materials as active layers. Meanwhile the issues associated with interface stability and charge transport/collection could be overcome.

Acknowledgements

Financial support from Academic Research Fund (RGM 44/06) of Ministry of Education, Singapore is gratefully acknowledged. Calculations at WFU were supported by DOE through Grant number DE-FG02-07ER46428.

Appendix A. Supporting information

Supplementary data associated with this article can be found in the online version at doi:10.1016/j.solmat.2010.11.023.

References

[1] F.C. Krebs, All solution roll-to-roll processed polymer solar cells free from indium–tin–oxide and vacuum coating steps, Org. Electron. 10 (2009) 761–768.
[2] F.C. Krebs, Fabrication and processing of polymer solar cells: a review of printing and coating techniques, Sol. Energy Mater. Sol. Cells 93 (2009) 394–412.
[3] D.W. Zhao, W.H. Tang, L. Ke, S.T. Tan, X.W. Sun, Efficient bulk heterojunction solar cells with poly 2,7-(9,9-dihexylfluorene)-alt-bithiophene and 6.6-phenyl c61 butyric acid methyl ester blends and their application in tandem cells, ACS Appl. Mater. Interfaces 2 (2010) 829–837.
[4] F. Zhang, A. Vollmer, J. Zhang, Z. Xu, J.P. Rabe, N. Koch, Energy level alignment and morphology of interfaces between molecular and polymeric organic semiconductors, Org. Electron. 8 (2007) 606–614.
[5] F.C. Krebs, S.A. Gevorgyan, J. Alstrup, A roll-to-roll process to flexible polymer solar cells: model studies, manufacture and operational stability studies, J. Mater. Chem. 19 (2009) 5442–5451.
[6] W.L. Ma, C.Y. Yang, X. Gong, K. Lee, A.J. Heeger, Thermally stable, efficient polymer solar cells with nanoscale control of the interpenetrating network morphology, Adv. Funct. Mater. 15 (2005) 1617–1622.
[7] G. Li, V. Shrotriya, J.S. Huang, Y. Yao, T. Moriarty, K. Emery, Y. Yang, High-efficiency solution processable polymer photovoltaic cells by self-organization of polymer blends, Nat. Mater. 4 (2005) 864–868.
[8] M. Jorgensen, K. Norrman, F.C. Krebs, Stability/degradation of polymer solar cells, Sol. Energy Mater. Sol. Cells 92 (2008) 686–714.
[9] M. Helgesen, R. Sondergaard, F.C. Krebs, Advanced materials and processes for polymer solar cell devices, J. Mater. Chem. 20 (2010) 36–60.
[10] E. Bundgaard, F.C. Krebs, Low band gap polymers for organic photovoltaics, Sol. Energy Mater. Sol. Cells 91 (2007) 954–985.
[11] W.Z. Cai, X. Gong, Y. Cao, Polymer solar cells: recent development and possible routes for improvement in the performance, Sol. Energy Mater. Sol. Cells 94 (2010) 114–127.
[12] L.M. Chen, Z.R. Hong, G. Li, Y. Yang, Recent progress in polymer solar cells: manipulation of polymer: fullerene morphology and the formation of efficient inverted polymer solar cells, Adv. Mater. 21 (2009) 1434–1449.
[13] X.N. Yang, J. Loos, S.C. Veenstra, W.J.H. Verhees, M.M. Wienk, J.M. Kroon, M.A.J. Michels, R.A.J. Janssen, Nanoscale morphology of high-performance polymer solar cells, Nano Lett. 5 (2005) 579–583.
[14] H. Hoppe, N.S. Sariciftci, Morphology of polymer/fullerene bulk heterojunction solar cells, J. Mater. Chem. 16 (2006) 45–61.
[15] L.M. Chen, Z. Xu, Z.R. Hong, Y. Yang, Interface investigation and engineering—achieving high performance polymer photovoltaic devices, J. Mater. Chem. 20 (2010) 2575–2598.
[16] S.K. Hau, H.L. Yip, N.S. Baek, J.Y. Zou, K. O'Malley, A.K.Y. Jen, Air-stable inverted flexible polymer solar cells using zinc oxide nanoparticles as an electron selective layer, Appl. Phys. Lett. 92 (2008) 253301.
[17] S.K. Hau, H.L. Yip, H. Ma, A.K.Y. Jen, High performance ambient processed inverted polymer solar cells through interfacial modification with a fullerene self-assembled monolayer, Appl. Phys. Lett. 93 (2008) 233304.
[18] C.S. Kim, S.S. Lee, E.D. Gomez, J.B. Kim, Y.L. Loo, Transient photovoltaic behavior of air-stable, inverted organic solar cells with solution-processed electron transport layer, Appl. Phys. Lett. 94 (2009) 113302.
[19] D.W. Zhao, P. Liu, X.W. Sun, S.T. Tan, L. Ke, A.K.K. Kyaw, An inverted organic solar cell with an ultrathin Ca electron-transporting layer and MoO_3 hole-transporting layer, Appl. Phys. Lett. 95 (2009) 153304.
[20] A.K.K. Kyaw, X.W. Sun, C.Y. Jiang, G.Q. Lo, D.W. Zhao, D.L. Kwong, An inverted organic solar cell employing a sol–gel derived ZnO electron selective layer and thermal evaporated MoO_3 hole selective layer, Appl. Phys. Lett. 93 (2008) 221107.
[21] S.K. Hau, H.L. Yip, O. Acton, N.S. Baek, H. Ma, A.K.Y. Jen, Interfacial modification to improve inverted polymer solar cells, J. Mater. Chem. 18 (2008) 5113–5119.
[22] D.W. Zhao, S.T. Tan, L. Ke, P. Liu, A.K.K. Kyaw, X.W. Sun, G.Q. Lo, D.L. Kwong, Optimization of an inverted organic solar cell, Sol. Energy Mater. Sol. Cells 94 (2010) 985–991.
[23] R. Hausermann, E. Knapp, M. Moos, N.A. Reinke, T. Flatz, B. Ruhstaller, Coupled optoelectronic simulation of organic bulk-heterojunction solar cells: parameter extraction and sensitivity analysis, J. Appl. Phys. 106 (2009) 104507.
[24] Y. Li, E.D. Peterson, H. Huang, M. Wang, D. Xue, W. Nie, W. Zhou, D.L. Carroll, Tube-based geometries for organic photovoltaics, Appl. Phys. Lett. 96 (2010) 243505.
[25] Y. Li, W. Zhou, D. Xue, J.W. Liu, E.D. Peterson, W.Y. Nie, D.L. Carroll, Origins of performance in fiber-based organic photovoltaics, Appl. Phys. Lett. 95 (2009) 203503.
[26] A. Hadipour, B. de Boer, J. Wildeman, F.B. Kooistra, J.C. Hummelen, M.G.R. Turbiez, M.M. Wienk, R.A.J. Janssen, P.W.M. Blom, Solution-processed organic tandem solar cells, Adv. Funct. Mater 16 (2006) 1897–1903.
[27] A.G.F. Janssen, T. Riedl, S. Hamwi, H.H. Johannes, W. Kowalsky, Highly efficient organic tandem solar cells using an improved connecting architecture, Appl. Phys. Lett. 91 (2007) 073519.
[28] J.Y. Kim, K. Lee, N.E. Coates, D. Moses, T.Q. Nguyen, M. Dante, A.J. Heeger, Efficient tandem polymer solar cells fabricated by all-solution processing, Science 317 (2007) 222–225.
[29] J.G. Xue, S. Uchida, B.P. Rand, S.R. Forrest, Asymmetric tandem organic photovoltaic cells with hybrid planar-mixed molecular heterojunctions, Appl. Phys. Lett. 85 (2004) 5757.
[30] D.W. Zhao, X.W. Sun, C.Y. Jiang, A.K.K. Kyaw, G.Q. Lo, D.L. Kwong, Efficient tandem organic solar cells with an Al/MoO_3 intermediate layer, Appl. Phys. Lett. 93 (2008) 083305.
[31] D.W. Zhao, X.W. Sun, C.Y. Jiang, A.K.K. Kyaw, G.Q. Lo, D.L. Kwong, An efficient triple-tandem polymer solar cell, IEEE Electron Device Lett. 30 (2009) 490–492.
[32] M.K. Siddiki, J. Li, D. Galipeau, Q.Q. Qiao, A review of polymer multijunction solar cells, Energy Environ. Sci. 3 (2010) 867–883.
[33] O. Hagemann, M. Bjerring, N.C. Nielsen, F.C. Krebs, All solution processed tandem polymer solar cells based on thermocleavable materials, Sol. Energy Mater. Sol. Cells 92 (2008) 1327–1335.
[34] A. Hadipour, B. de Boer, P.W.M. Blom, Organic tandem and multi-junction solar cells, Adv. Funct. Mater 18 (2008) 169–181.
[35] G. Dennler, H.J. Prall, R. Koeppe, M. Egginger, R. Autengruber, N.S. Sariciftci, Enhanced spectral coverage in tandem organic solar cells, Appl. Phys. Lett. 89 (2006) 073502.
[36] K. Kawano, N. Ito, T. Nishimori, J. Sakai, Open circuit voltage of stacked bulk heterojunction organic solar cells, Appl. Phys. Lett. 88 (2006) 073514.

[37] J. Gilot, M.M. Wienk, R.A.J. Janssen, Double and triple junction polymer solar cells processed from solution, Appl. Phys. Lett. 90 (2007) 143512.
[38] S. Sista, M.H. Park, Z.R. Hong, Y. Wu, J.H. Hou, W.L. Kwan, G. Li, Y. Yang, Highly efficient tandem polymer photovoltaic cells, Adv. Mater. 22 (2010) 380–383.
[39] X.W. Sun, D.W. Zhao, L. Ke, A.K.K. Kyaw, G.Q. Lo, D.L. Kwong, Inverted tandem organic solar cells with MoO_3/Ag/Al/Ca intermediate layer, Appl. Phys. Lett. 97 (2010) 053303.
[40] L.A.A. Pettersson, L.S. Roman, O. Inganas, Modeling photocurrent action spectra of photovoltaic devices based on organic thin films, J. Appl. Phys. 86 (1999) 487–496.
[41] A.J. Moule, J.B. Bonekamp, K. Meerholz, The effect of active layer thickness and composition on the performance of bulk-heterojunction solar cells, J. Appl. Phys. 100 (2006) 094503.
[42] A.J. Moule, K. Meerholz, Interference method for the determination of the complex refractive index of thin polymer layers, Appl. Phys. Lett. 91 (2007) 061901.
[43] J.Y. Kim, S.H. Kim, H.H. Lee, K. Lee, W.L. Ma, X. Gong, A.J. Heeger, New architecture for high-efficiency polymer photovoltaic cells using solution-based titanium oxide as an optical spacer, Adv. Mater. 18 (2006) 572–576.
[44] A. Hadipour, B. de Boer, P.W.M. Blom, Solution-processed organic tandem solar cells with embedded optical spacers, J. Appl. Phys. 102 (2007) 074506.
[45] J. Gilot, I. Barbu, M.M. Wienk, R.A.J. Janssen, The use of ZnO as optical spacer in polymer solar cells: theoretical and experimental study, Appl. Phys. Lett. 91 (2007) 113520.
[46] A. Roy, S.H. Park, S. Cowan, M.H. Tong, S.N. Cho, K. Lee, A.J. Heeger, Titanium suboxide as an optical spacer in polymer solar cells, Appl. Phys. Lett. 95 (2009) 013302.
[47] R. Schueppel, R. Timmreck, N. Allinger, T. Mueller, M. Furno, C. Uhrich, K. Leo, M. Riede, Controlled current matching in small molecule organic tandem solar cells using doped spacer layers, J. Appl. Phys. 107 (2010) 044503.
[48] A.K. Pandey, P.E. Shaw, I.D.W. Samuel, J.M. Nunzi, Effect of metal cathode reflectance on the exciton-dissociation efficiency in heterojunction organic solar cells, Appl. Phys. Lett. 94 (2009) 103303.
[49] C. Tao, S.P. Ruan, X.D. Zhang, G.H. Xie, L. Shen, X.Z. Kong, W. Dong, C.X. Liu, W.Y. Chen, Performance improvement of inverted polymer solar cells with different top electrodes by introducing a MoO_3 buffer layer, Appl. Phys. Lett. 93 (2008) 193307.
[50] F. Monestier, J.J. Simon, P. Torchio, L. Escoubas, F. Florya, S. Bailly, R. de Bettignies, S. Guillerez, C. Defranoux, Modeling the short-circuit current density of polymer solar cells based on P3HT: PCBM blend, Sol. Energy Mater. Sol. Cells 91 (2007) 405–410.
[51] D.W. Sievers, V. Shrotriya, Y. Yang, Modeling optical effects and thickness dependent current in polymer bulk-heterojunction solar cells, J. Appl. Phys. 100 (2006) 114509.
[52] H. Hoppe, N. Arnold, N.S. Sariciftci, D. Meissner, Modeling the optical absorption within conjugated polymer/fullerene-based bulk-heterojunction organic solar cells, Sol. Energy Mater. Sol. Cells 80 (2003) 105–113.
[53] H. Hoppe, N.S. Sariciftci, D. Meissner, Optical constants of conjugated polymer/fullerene based bulk-heterojunction organic solar cells, Mol. Cryst. Liq. Cryst. 385 (2002) 233–239.
[54] T.S. Sian, G.B. Reddy, Optical, structural and photoelectron spectroscopic studies on amorphous and crystalline molybdenum oxide thin films, Sol. Energy Mater. Sol. Cells 82 (2004) 375–386.
[55] Refractive Index. Info. database 〈http://refractiveindex.info〉.
[56] Yuan Li, Organic Photovoltaics Analysis Platform (OPVAP), USA 〈www.OPVAP.inwake.com〉.